

# Molecular Dynamics simulation of evaporation processes of fluid bridges confined in slit-like pore

Katarzyna Bucior, Leonid Yelash, and Kurt Binder

*Institut für Physik, Johannes Gutenberg-Universität*

*D-55099 Mainz, Staudinger Weg 7, Germany*

## Abstract

A simple fluid, described by point-like particles interacting via the Lennard-Jones potential, is considered under confinement in a slit geometry between two walls at distance  $L_z$  apart for densities inside the vapor-liquid coexistence curve. Equilibrium then requires the coexistence of a liquid “bridge” between the two walls, and vapor in the remaining pore volume. We study this equilibrium for several choices of the wall-fluid interaction (corresponding to the full range from complete wetting to complete drying, for a macroscopically thick film), and consider also the kinetics of state changes in such a system. In particular, we study how this equilibrium is established by diffusion processes, when a liquid is inserted into an initially empty capillary (partial or complete evaporation into vacuum), or when the volume available for the vapor phase increases. We compare the diffusion constants describing the rates of these processes in such inhomogeneous systems to the diffusion constants in the corresponding bulk liquid and vapor phases.

## 1 Introduction

Fluids confined into pores with diameters on the micrometer scale down to the nanometer scale are important in a variety of contexts: they control the properties of wet granular matter [1], they play a role for oil recovery from porous rocks or compactified sands [2], separation processes in zeolites [3], drying processes of food, wood, or other porous solids [4], nanofluidic devices using fluids in carbon nanotubes [5], dip-pen nanolithography [6], nanolubrication [7], fluid transport in living organisms [8], etc. [9–12]. Many of these applications involve nonequilibrium processes such as the flow of fluids in confined geometry, imbibition of fluids into pores (e.g. [13–17]), surface-directed spinodal decomposition (e.g. [18–22]) if one considers binary fluid mixtures, or evaporation processes of fluids [4]. While the evaporation process of bulk liquids (across a flat interface) [23–29] and of small droplets [30–33] has been studied extensively, liquid-vapor transitions under confinement have been mostly studied emphasizing equilibrium aspects only [9,12,34–41]. Note that we do not discuss here the inverse process (nucleation of fluid droplets from the vapor in confined systems, see e.g. [42,43]), and we consider neither the structure (and possible rupture) of non-volatile confined liquid bridges [44,45], nor liquid-vapor systems confined by patterned surfaces (see e.g. [44–47]).

In the present paper we wish to contribute to the understanding of the kinetics of nonequilibrium processes of confined fluids considering the partial (or complete) evaporation of liquid bridges, resulting from changes of external conditions, using Molecular Dynamics methods [48–50] to simulate a simple Lennard-Jones fluid confined between parallel walls. We are particularly interested in elucidating the consequences of the inhomogeneity of the structure of the liquid bridges (depending on the drying/wetting boundary conditions at the confining walls [9,51–56], there is also an inhomogeneity of the system in the  $z$ -direction perpendicular to the walls) on the evaporation processes.

In the following section, we shall describe the model that is simulated and give a few comments on the simulation method, and the quantities, that are computed. In Sec. III, we describe the static structure of the liquid bridges (as well as the regions of the slit pore where the vapor phase dominates), for various choices of the strength of the interaction between the fluid particles and the walls, relating the observed interfacial behavior to theoretical concepts about wetting. In Sec IV, we present some discussion on the transport behavior of pure coexisting vapor and liquid phases, under confinement in the slit pores. Sec. V then considers the relaxation of the system after suitable parameter changes that lead to partial (or even complete) evaporation of the liquid bridges present in the slit pores. The kinetic evolution towards the new (inhomogeneous!) equilibrium is documented in detail. Finally, Sec. VI contains our conclusions, and gives an outlook on future work.

## 2 Model and Simulation Method

In this study we are not addressing a particular material but rather wish to gain insight into the generic behavior of simple fluids (such as  $\text{CH}_4$ ,  $\text{CO}_2$ , etc.) under confinement. Thus, we describe the fluid particles as point-like, interacting via truncated and shifted Lennard-Jones potential,

$$\begin{aligned} U(r) &= U_{LJ}(r) - U_{LJ}(r_{\text{cut}}), \\ U_{LJ} &= 4\varepsilon[(\sigma/r)^{12} - (\sigma/r)^6], \end{aligned} \tag{1}$$

with  $r_{\text{cut}} = 2r_{\text{min}}$ ,  $r_{\text{min}} = 2^{1/6}\sigma$ . Note that  $U_{LJ}(r_{\text{cut}})$  is chosen such that  $U(r)$  is everywhere continuous, with  $U(r \geq r_{\text{cut}}) = 0$ . Mognetti et al. [57] have shown that this model can describe fairly well the coexistence curves, vapor pressure, and interfacial tension of molecules like  $\text{CH}_4$  or even  $\text{C}_3\text{H}_8$  over a temperature regime from about  $0.7 T_c$  to  $T_c$ , when  $\varepsilon$  and  $\sigma$  in Eq. (1) are adjusted such that the critical temperature  $T_c$  and critical density  $\rho_c$  are correctly reproduced by the model ( $\rho_c$ ,  $T_c$  can be accurately estimated from the model by careful finite size scaling analyses of Monte Carlo simulations of the model in the grand-canonical ensemble, as discussed elsewhere [57, 58]). Even for  $\text{CO}_2$  this model yields a fair description [58], although better accuracy can be obtained for this molecule if the quadrupolar interaction is included [57], but this is out of consideration here.

For a fluid confined in a slit pore geometry, it is also necessary to specify the boundary conditions created by the planar walls confining the thin film. Following Ref. [22], we choose an atomistic description of these walls, setting particles on a regular (and rigid) triangular lattice of lattice spacing  $\sigma$ , in the  $(x, y)$  plane at  $z = 1$  and at  $z = L_z - 1$  (note that henceforth lengths are measured in units of  $\sigma$  throughout). The interaction between wall particles and fluid particles is chosen also of the form of Eq. (1), but the

energy parameter  $\varepsilon$  is replaced by  $\varepsilon_w = \zeta\varepsilon$  with  $\zeta$  being varied from  $\zeta = 0.1$  to  $\zeta = 0.9$ . An additional simulation was made where we made the interaction between the wall and fluid particles purely repulsive: in this case, the wall particles were placed in the planes  $z = 0.5$  and  $z = L_z - 0.5$ , respectively, and  $r_{\text{cut}} = r_{\text{min}}$  was chosen in Eq. (1), so that  $U_{LJ}(r_{\text{cut}}) = 0$  then. In this case,  $\varepsilon_w = \varepsilon$  was used. Henceforth, we shall also measure temperature in LJ units (i.e.,  $\varepsilon \equiv 1$ ,  $k_B \equiv 1$ ). Typical linear dimensions in  $x$  and  $y$  directions parallel to the walls were at least  $L_x = 30$ ,  $L_y = 15$ , choosing periodic boundary conditions in these directions, and also  $L_z = 15$  or  $L_z = 16$  was chosen: the reason for choosing  $L_x = 2L_y$  is that then the vapor-liquid interfaces that form in the slit pore for suitable total densities will be oriented in the  $yz$ -plane, perpendicular to the  $x$ -direction; to minimize the interfacial free energy cost. No inhomogeneity in  $y$ -direction is then expected, and hence averages of density profiles along the  $y$ -direction can be taken. When liquid bridges occur, the density distribution must then depend on both the  $x$  and the  $z$  coordinates.

Of course, the choice of the linear dimensions in a computer simulation is a subtle matter, due to finite size effects [50, 59]. While the finite size effects associated with the two walls defining the finite width of the slit pore are the physically significant effect that we wish to study, finite size effects due to too small values of  $L_x$  and  $L_y$  are simulation artefacts, since the real systems (if they are finite of nanoscopic size in  $x$  and  $y$  direction as well) would have other boundary effects rather than periodic boundary conditions. Choice of the latter makes sense to simulate a system that is truly macroscopic in  $x$  and  $y$  directions, of course. While homogeneous systems (containing a single phase) typically approach the thermodynamic limit rapidly, at least for temperatures or densities outside of the critical region [59], this is not always the case for systems exhibiting phase coexistence within a finite simulation box [38, 59–61]. In particular, when we have a liquid slab with two interfaces (perpendicular to the  $x$ -direction) in our system, we expect that both interfaces have a finite thickness: the standard description postulates an “intrinsic thickness”  $\ell = 2\xi$ , where  $\xi$  is the correlation length of density fluctuations in the liquid, broadened by capillary waves [62]. While  $\xi$  diverges near the critical point of the fluid,  $\xi \approx \sigma$  if we are far below criticality. However, since the broadening caused by capillary waves increases logarithmically with  $L_y$ , an interfacial thickness of  $2\sigma$  to  $4\sigma$  must be typically expected. However, the two parallel interfaces separating the liquid bridge from the surrounding vapor in the simulation box need to be at a distance  $L \gg \ell$ , in order that interactions between these interfaces are negligible. Because of the periodic boundary condition in  $x$  direction,  $L_x$  must exceed  $L$  by a factor of 2 or 3 as well. In order to test for possible finite size effects, we have done part of our simulations with larger linear dimensions, up to  $L_x = 90$ .

All simulations were carried out using Molecular Dynamics methods in the framework of the NVT ensemble. Applying the ESPResSO package [63], the Newton equations of motion are integrated via the Velocity Verlet algorithm [48–50], using a time step  $\delta t = 0.002\tau$  where the MD time unit  $\tau$  is defined as  $\tau = \sigma(m/\varepsilon)^{1/2}$ , where the mass  $m = 1$  is chosen for the molecules. Temperature was controlled by using the Langevin thermostat and  $T^* = 0.9366$  was chosen throughout.

In order to produce initial states containing liquid bridges surrounded by vapor, we first equilibrated dense fluids (average density  $\rho \approx 0.5813$ ) in a small box with  $L_x = 30$ ,  $L_y = 20$ ,  $L_z = 16$  and 9000 particles. The density of the fluid is calculated as  $\rho = N\sigma^3/V$ , where  $N$ - number of particles and  $V = L_x L_y (L_z - 2)$  for attractive walls, and  $V = L_x L_y (L_z - 1)$  for repulsive walls. After an equilibration run extending over at least  $100\tau$  we put this liquid in the center of a box with linear dimension  $L_x = 60$ ,  $L_y = 20$ ,  $L_z = 16$ , and simulate this system over a time interval of  $20000\tau$ . The initial stages of such

a run serve as a simulation of liquid evaporation into vacuum. For time  $t > 5000\tau$ , the liquid bridge is essentially well equilibrated with respect to the coexisting vapor, and then averages of the density profiles  $\rho(x, z)$  are taken.

### 3 Static structure of the liquid bridges

In order to obtain an overview of the behavior, Figs. 1, 2 present contour plots of the density distribution  $\rho(x, z)$  for systems of sizes  $L_x = 60, L_y = 20$  and  $L_z = 16$  and  $L_x = 90, L_y = 20$  and  $L_z = 16$ , respectively. In both cases the color coding goes from dark blue, corresponding to  $\rho = 0$ , to red, corresponding to  $\rho = 0.65$ , as indicated by the bar on the top of each figure. The individual pictures illustrate the variation with  $\varepsilon_w$ , while  $N=9000$  particles were used throughout. Thus, the average density in Fig. 1 is  $\bar{\rho} \approx 0.291$  (when we use the maximum available volume  $60 \times 20 \times 16$ , remembering that the wall particles are fixed at  $z = 1$  and at  $z = L_z - 1 = 15$ , respectively), while in Fig. 2 it is only  $\bar{\rho} \approx 0.194$  due to the larger  $L_x = 90$ . Note that at the chosen temperature  $T^* = 0.9366$  the coexisting vapor and liquid densities are  $\rho_v = 0.109$ ,  $\rho_\ell = 0.565$ ; thus, if the density distribution would be homogeneous in the  $z$ -direction across the slit pore, we could simply expect a two-phase equilibrium with a volume fraction  $X = (\bar{\rho} - \rho_v)/(\rho_\ell - \rho_v)$  of the liquid phase, and the vapor-liquid interfaces would simply show up as straight lines in the  $z$ -direction in Figs. 1, 2. However, due to the particle-wall interactions, a nontrivial inhomogeneity of the density distribution in the  $z$ -direction results, which readily shows up in Figs. 1, 2.

For small  $\varepsilon_w$  one sees in Figs. 1, 2 clear evidence of drying behavior: rather than observing a liquid bridge connecting the confining walls, there occurs in the center of the slit pore a free standing elliptic liquid cylinder periodic in  $y$  direction, separated by the vapor phase that has intruded in between the liquid and the wall. It is obvious that the vapor-liquid interfaces in the  $z$ -direction actually are distinctly narrower than along the  $x$ -direction. This effect in fact is expected, of course, since confinement has a strong constraining effect on interfacial fluctuations in the  $z$ -direction, while the finite size  $L_x$  in  $x$ -direction has much less effect to constrain the interfaces.

While in the case of  $L_x = 60$  the linear dimension of the liquid slab in the  $x$ -direction is large enough, so that in the center of the slab the dependence of any physical properties on the  $x$ -coordinate is negligible small, for  $\varepsilon_w = 0.1$  to  $\varepsilon_w = 0.4$ , this clearly is not true for  $L_x = 90$ : as  $\varepsilon_w$  increases the linear dimension of the liquid slab along the  $x$ -axis gets smaller and smaller (since a larger fraction of particles now stays in the gas phase, and for larger  $\varepsilon_w$  more and more particles get adsorbed at the walls). The elliptical shape of the contours of constant density in Fig. 2 clearly imply that the two interfaces separating vapor from liquid and then liquid from vapor along the  $x$ -direction interact with each other. We do expect that such thin liquid slabs with interacting interfaces can evaporate much easier than thick slabs, where these interfaces are separated by a thick region of bulk liquid from each other.

For  $\varepsilon_w = 0.5$  the vapor no longer can intrude in between the liquid slab and the walls, rather the liquid-vapor interface is “cut off” by the walls. In the region from  $\varepsilon_w = 0.61$  to  $\varepsilon_w = 0.65$  (the last one not shown), the vapor-liquid interface seems to run almost straight along the  $z$ -direction, implying (in the macroscopic limit of very thick slabs) a contact angle of  $\theta = 90^\circ$ , while for  $\varepsilon_w \leq 0.5$  one clearly can speak about a contact angle exceeding  $90^\circ$  (as long as  $\theta < 180^\circ$  one speaks about “incomplete drying”, while a thick vapor region in between the walls and the fluid slab should correspond to  $\theta = 180^\circ$ , complete

drying). For  $\varepsilon_w \geq 0.7$  the shape of the liquid slabs, connecting the confining surfaces in Fig. 1 suggest contact angles  $\theta < 90^\circ$ , corresponding to incomplete wetting conditions. However, we emphasize that for nanoscopically thin films the concept of a contact angle is somewhat ill-defined, since it requires that over distances much larger than the interface thickness its curvature is negligible. This condition clearly is not satisfied here. This lack of a precise definition of the contact angle in nanoscopically thin slits corresponds to the fact that wetting transitions in such geometries show finite-size rounding [64].

One can also recognize from Fig. 1 for  $\varepsilon \geq 0.61$  a pronounced layering effect near the walls. This layering effect obscures the “contact region” where the interface meets the wall. For  $\varepsilon = 0.9$ , the walls are coated already with precursors of wetting layers, indicative of the vicinity of the rounded wetting transition. Note, however, that for  $\varepsilon_w = 0.9$  the total particle number in the system does not suffice to allow the formation of a well-defined liquid bridge reaching bulk liquid density in the center of the system. For the larger system ( $L_x = 90$ ), the liquid bridge already has disappeared somewhere in between  $\varepsilon_w = 0.65$  and  $0.70$ , since there is enough space for all the particles to either stay in the vapor or get adsorbed in the precursors of the wetting layers near the walls.

At this point, we mention that in our evaluation of simulation data we always have fixed the center of mass of all the particles right in the center of the slit pore (i.e., at  $x = L_x/2$ ). Due to the periodic boundary condition in  $x$ -direction, translational invariance in  $x$ -direction is implied of course. Thus, fixing the center of mass is a convenient precaution against the diffusion of the liquid along the  $x$ -axis as a whole, which would smear out the density inhomogeneity on average, of course; such an undesirable effect could obscure corresponding experimental observations, where one cannot control the position of the liquid slab as easily.

Fig. 3 shows two selected profiles  $\rho(x_1, z)$  and  $\rho(x_2, z)$  in more detail, choosing  $x_1$  such that a cut through the center of the liquid slab is performed, while  $x_2$  is chosen to monitor the density profile through the slit pore in the vapor region, far away from the liquid slab. In each part of Fig. 3 there are presented plots of density for 2 system sizes:  $L_x = 60, L_y = 20, L_z = 16$  (solid lines) and  $L_x = 90, L_y = 20, L_z = 16$  (lines with circles). Density profiles for both box sizes  $L_x$  overlap for values of parameter  $\varepsilon_w < 0.65$ . One can see that in the region of incomplete drying ( $\varepsilon_w = 0.1$ ) the liquid density decreases almost linearly with  $z$  over a significant region of  $z$  when one approaches either wall. For  $\varepsilon_w = 0.3$  there is already evidence of a layering effect in the density profile. While in the vapor phase the density is higher in the layer adjacent to the wall than in the center of the slit pore, in the liquid phase the behavior is different - the density in this region is significantly higher than in the layer close to the wall. However for  $\varepsilon_w = 0.5$  the density in the center of the slit pore is already lower than in the layers adjacent to the walls. For  $\varepsilon_w \geq 0.7$  the layering effect is even more pronounced, leading to a density that is higher even in the second layer adjacent to the wall than in the center of the slit pore.

In order to characterize the behavior more precisely in the region of those values of  $\varepsilon_w$  where the interfaces between vapor and liquid are approximately planar, Fig. 4 presents magnified plots of the profiles  $\rho(x_1, z)$  and  $\rho(x_2, z)$  vs.  $z$  where 5 values of  $\varepsilon_w$  from  $\varepsilon_w = 0.4$  to  $\varepsilon_w = 0.65$  are shown. This situation where the contact angle  $\theta = 90^\circ$  is the “transition” from incomplete drying to incomplete wetting [51–56]. We emphasize, however, that even in the thermodynamic limit ( $L_z \rightarrow \infty$ ) this “transition” is a completely smooth change, unlike the wetting transition (where  $\theta \rightarrow 0$ ) or the drying transition (where  $\theta \rightarrow 180^\circ$ ), which become sharp thermodynamic transitions (singularities of the surface excess

free energies associated with the walls [51–56]) in this limit. We also note that the density profile in the vapor phase becomes almost horizontal already for  $\varepsilon_w = 0.4$ , while the density profile in the center of the liquid slab becomes horizontal (in the regime of  $z$  where the layering oscillations have died out) only for  $\varepsilon_w \approx 0.65$ , however. Thus, for  $\varepsilon_w = 0.55$  to  $\varepsilon_w = 0.61$ , where we approximately have  $\theta = 90^\circ$ , there is a clear enhancement of the density in the first two layers adjacent to the walls. Of course, it would be desirable to study these behaviors varying also  $L_z$  over a wide range, but this has not been attempted since it would involve a major computational effort. We emphasize again, that our simulations for these rather thin slit pores are not suitable to precisely estimate where drying and wetting transitions occur {which would show up as macroscopically thick vapor layers at the walls for the liquid profile  $\rho(x_1, z)$  or liquid layers at the walls for the vapor profile  $\rho(x_2, z)$ , respectively}.

Another caveat that must be made with respect to the quantitative analysis of our results concern finite size effects associated with the linear dimension  $L_x$ . Comparing e.g. the curves  $\rho(x_1, z)$  for  $\varepsilon_w = 0.65$  for  $L_x = 60$  and  $L_x = 90$  (cf. Fig. 3) we see that for  $L_x = 90$  the density clearly is smaller: since the total particle number was  $N=9000$  in both cases, more particles were required for  $L_x = 90$  to create a vapor phase with the proper density in the box volume, and the remaining particles were only sufficient for a liquid slab that was too thin to reach the bulk liquid density in its center. This fact is emphasized in Fig. 5, where the density profiles  $\bar{\rho}(x) = \int_1^{L_z-1} \rho(x, z) dz / (L_z - 2)$  are shown for 6 values of  $\varepsilon_w$ . While for  $L_x = 60$  there is an (albeit small) region of  $x$  where  $\bar{\rho}(x)$  is flat in the center of the liquid slab, for  $L_x = 90$  the right and left interfaces clearly are no longer well separated from each other. This effect becomes more dramatic, of course, if one reduces the total number of particles in the slit pore (cf. the curve for  $N = 4500$ ,  $L_x = 45$  and  $\varepsilon_w = 0.6$ , as an example).

Note that the equilibrium conditions for phase coexistence under confinement are equal temperature and equal chemical potential throughout our systems; the local pressure (and its change due to the curvature of the interfaces in Figs. 1 and 2) does not play any role in characterizing the equilibrium conditions here.

We conclude this section by emphasizing that the purpose of our paper is not the study of wetting and drying transitions, but the study of liquid-vapor coexistence (and evaporation phenomena) in slit pores that have nanoscopically small linear dimensions. But the purpose of the present section was to clarify the equilibrium properties of phase coexistence under such conditions, and to give some hints about the finite size effects that one needs to understand for a proper interpretation of the observed behavior.

## 4 Effect of liquid-vapor coexistence in slit pores on the transport behavior

Choosing a system in a cubic box geometry of size  $L \times L \times L$  and periodic boundary conditions, it is straightforward to obtain the self-diffusion constants of the particles from their mean-square displacement as a function of time, using the Einstein relation [48, 49]. This diffusion constant in the bulk (b) hence becomes

$$D_b = \lim_{t \rightarrow \infty} [\langle [\vec{r}_i(t) - \vec{r}_i(0)]^2 \rangle] / (6t). \quad (2)$$

Here is understood that the average  $\langle \dots \rangle$  includes an average over all particles (labeled by index  $i$

in Eq. (2)) in the system, as well as an average over the origin of time (there exists time translation invariance in thermal equilibrium, of course). Using Eq. (2), the diffusion constants of bulk vapor and liquid have been obtained, at vapor-liquid coexistence

$$D_{v,b} = 1.059 \quad , \quad D_{\ell,b} = 0.173 . \quad (3)$$

When we consider a fluid confined in a slit pore, one needs to consider the following effects: first of all, the mean-square displacement can diverge only in the  $x$ - and  $y$ -directions, but not in the  $z$ -direction perpendicular to the walls. This type of anisotropy of diffusion in equilibrium was also studied by Bock et al. [65] for a system with patterned walls. For every thick slit pores in pure vapor and liquid phases, where the relative effect of the walls on the diffusion constant can be neglected, we expect that the diffusion constants in the slit ( $s$ ) pore become

$$D_{v,s} = (2/3)D_{v,b} \quad , \quad D_{\ell,s} = (2/3)D_{\ell,b} . \quad (4)$$

However, the finite linear dimension of the slit pore in the  $z$ -direction does introduce slow transients in the behavior of the mean-square displacement: a particle starting in the center of the slit pore can also diffuse into the  $z$ -direction over a distance  $L_z/2$  before the confinement becomes effective. In fact, such a particle hence can diffuse like in a three-dimensional bulk system over a time  $t_D = (L_z/2)^2/(6D_b)$  before the quasi-two-dimensional diffusion sets in. For this reason, we have defined in terms of the cartesian coordinates  $x_i(t)$ ,  $y_i(t)$  and  $z_i(t)$  some effective time-dependence diffusion constants as follows

$$D(t) = \langle [x_i(t) - x_i(0)]^2 + [y_i(t) - y_i(0)]^2 + [z_i(t) - z_i(0)]^2 \rangle / (6t) \quad , \quad (5)$$

$$D^{(xy)}(t) = \langle [x_i(t) - x_i(0)]^2 + [y_i(t) - y_i(0)]^2 \rangle / (4t) \quad , \quad (6)$$

$$D^{(xz)}(t) = \langle [x_i(t) - x_i(0)]^2 + [z_i(t) - z_i(0)]^2 \rangle / (4t) \quad , \quad (7)$$

and

$$D^{(yz)}(t) = \langle [y_i(t) - y_i(0)]^2 + [z_i(t) - z_i(0)]^2 \rangle / (4t) \quad . \quad (8)$$

As long as there do not occur any interfaces, the symmetry of the problem requires  $D^{(xz)}(t) = D^{(yz)}(t)$ , of course, and this symmetry is in fact nicely obeyed by the numerical data (Fig. 6). On the other hand, for  $t \ll t_D$  confinement is not effective, and then the time variation of  $D^{(xy)}(t)$ ,  $D^{(xz)}(t)$  and  $D^{(yz)}(t)$  is similar. However, at late times  $D^{(xy)}(t)$  converges to  $D_s$  while  $D^{(xz)}(t)$  and  $D^{(yz)}(t)$  converge to  $D_s/2$ , since at late times these mean-square displacements sample diffusion only in one direction. This leads to a maximum of  $D^{(xz)}(t)$  and  $D^{(yz)}(t)$  at intermediate times (Fig. 6). Also  $D(t)$  for the confined system exhibits a maximum at about the same time, while the time-dependence of  $D^{(xy)}(t)$  is always monotonic.

From Fig. 6 it is obvious that even in the bulk we must run the system over a time  $\tau \geq 10^2$  to reach saturation at the asymptotic values of  $D$ . The diffusion constant in the vapor is about 6 times larger than in the liquid as noted in Eq. (3), but the times for the mean-square displacements to converge to these values are about the same. In the bulk, no cartesian coordinate is distinguished, and hence

$D(t) = D^{(xy)}(t) = D^{(xz)}(t) = D^{(yz)}(t)$ . This symmetry properly indeed is rather nicely fulfilled, and this is only a test of the very good statistical accuracy of our data.

While for the confined liquid  $D^{(xy)}(t)$  follows rather closely the behavior of the bulk  $D(t)$ , for  $\varepsilon_w = 0.59$ , for the confined vapor  $D^{(xy)}(t)$  is significantly smaller than  $D(t)$ . Presumably, this is due to the fact that the vapor phase at  $\varepsilon_w = 0.59$  clearly is rather inhomogeneous (see Fig. 4).

The diffusion constants  $D(t)$  of the confined system settle down at  $\frac{2}{3}D^{(xy)}(t \rightarrow \infty)$  while the diffusion constants  $D^{(xz)}(t) = D^{(yz)}(t)$  settle down at  $\frac{1}{2}D^{(xy)}(t \rightarrow \infty)$ . These ratios  $2/3$ ,  $1/2$  trivially follow from the normalization of the mean-square displacements in Eqs. (5)- (8) and the fact that only mean square displacements of  $x$  and  $y$  coordinates diverge. Since the relaxation time  $\tau_D$ , defined above, which measures how long it takes for the particles to feel the confinement does scale inversely with the diffusion constant, it is plausible that it takes about 6 times longer in the liquid to reach the asymptotic values of  $D(t)$  and  $D^{(xy)}(t)$  than it does in the vapor phase. However, the absolute magnitude of these times is much larger than expected: using  $L_z/2 = 8$  we would estimate that in the liquid  $t_D$  is of the order of 100 only!

## 5 Simulation of Evaporation Processes

### 5.1 Evaporation of Liquid into Vacuum

In this section, we consider nonequilibrium relaxation processes where due to some change of external conditions the size of a liquid bridge shrinks. E.g., the lateral linear dimension available for the fluid suddenly increases (we shall not discuss how such a process could be physically realized in an experiment). Other conceivable changes of external parameters could involve changes of temperature, or of the wall-particle interaction, etc.

The first process that is studied is the evaporation of liquid into “vacuum”, i.e. we conceive the situation that a pore is completely filled with liquid, and due to a sudden change of some external conditions (e.g. a confining wall limiting the lateral extent of the pore in the  $x$ -direction is removed) additional pore volume becomes available. The first situation for which this process is considered refers to pore walls with a purely repulsive wall-particle interaction (see Sec. 2). In this case we chose an initial box with linear dimensions  $L_x = 30$ ,  $L_y = 15$ ,  $L_z = 15$ , walls being placed at  $z = 0.5$  and  $z = L_z - 0.5$ , respectively, and periodic boundary conditions are applied in  $x$  and  $y$  directions. This system then contains  $N = 4500$  particles so that the average density of the liquid in the simulation box is 0.388 while the density in the center of the box (for  $z \approx L_z/2$ ) is about 0.598. Then at time  $t = 0$  the periodic boundary condition in the  $x$ -direction is removed, and the system is placed into the center of a box that is twice as large in  $x$ -direction,  $L_x = 60$ , leaving all other linear dimensions and boundary conditions invariant. For times  $t > 0$  a periodic boundary condition in  $x$ -direction appropriate for  $L_x = 60$  is reintroduced. The system (which was in equilibrium and translationally invariant in  $x$ -direction for times  $t < 0$ ) now is far out of equilibrium, because there occurs “vacuum” (no fluid particles) for  $0 < x < 15$ ,  $45 < x < 60$ , while we have a fluid (inhomogeneous in  $z$ -direction because of the repulsive walls, of course) in the region from  $15 < x < 45$  while at  $x = 15$  and  $x = 45$  there occur sharp fluid-vacuum interfaces at  $t = 0$ . Figs. 7a-d show the resulting time evolution of the local density  $\rho(x, \bar{z}, t)$  where we have introduced layers 1,2,3,4,5 such that in layer 1  $\rho(x, z, t)$  is averaged from  $z = 0$  to  $z = 1.5$  as well as from  $z = 15$  to  $z = 13.5$ , in



layer 2 from  $z = 1.5$  to  $z = 3$  and from  $z = 13.5$  to  $z = 12$ , in layer 3 from  $z = 3$  to  $z = 4.5$  and from  $z = 12$  to  $z = 10.5$ , in layer 4 from  $z = 4.5$  to  $z = 6$  and from  $z = 10.5$  to  $z = 9$ , while layer 5 comprises the central part of the slit pore (from  $z = 6$  to  $z = 9$ ). Due to the strongly repulsive wall-fluid particle interaction, almost never any particles occur in layer 1, and hence only layers 2,3,4 and 5 are shown in Fig. 7. One can see that the interfacial profile in  $x$ -direction rapidly smoothens, and the density in the central region of the liquid slab also decreases as fluid particles evaporate and diffuse into the region of the vapor phase. It only takes a few hundred MD steps to establish full liquid-vapor equilibrium (with a homogeneous density of the vapor in  $x$ -direction, away from the liquid-vapor interfacial regions) as the comparison between curves for  $t = 500$  and  $t = 20000$  MD time steps shows. Note that the fluid particles that “populate” the volume region which in equilibrium form the vapor phase have to come from the interior of the liquid slab and move through the region where the liquid-vapor interface forms. The thickness of this interface gradually increases with time until the equilibrium interfacial thickness is reached and thus there occur values of  $x$  where the time evolution of the local density is nonmonotonic. Even for the density fully averaged in  $z$ -direction,  $\rho(x, t) = L_z^{-1} \int_0^{L_z} \rho(x, z, t) dz$ , a clear non-monotonic time evolution occurs for  $x = 13.5$  and  $x = 14.5$ . (Fig. 8). This happens because as the thickness of the liquid slab shrinks the interfacial profile moves inward, away from its initial position at  $x = 15$ , of course. Outside of the wings of the interfacial profile, e.g. for  $x = 10.5$ , there is a monotonous density increase while in the interior of the liquid slab there is a continuous density decrease.

Of course, one can also study how the density profiles in  $z$ -direction changes, at different location in  $x$ -direction along the pore (Fig. 9). One can see here that in the region where the vapor forms (Fig. 9a) there is a monotonic increase of density for all  $z$ , but the central region takes longest to equilibrate (for  $t = 200$  MD time units there is still a clear deviation from equilibrium). In the interfacial region, there is a pronounced overshoot of the density in the center of the pore, Fig. 9b, while inside the region when the liquid initially was situated there is a monotonic density decrease. This is large effect near the interfaces (Fig. 9c) and only a small effect in the central region of the liquid slab (Fig. 9d).

It is of similar interest to study this process when we introduce a non-zero fluid-wall interaction  $\varepsilon_w$  (Fig. 10), as has been studied (with respect to the thermal equilibrium aspects) already in Sec. 3. It is interesting to note that there is little effect of  $\varepsilon_w$  on the time evolution of the total density  $\rho(x, t)$  averaged over all distances  $z$  (Fig. 11), as long as the final equilibrium state still contains a thick liquid slab in the center of the film. This is the case still for  $\varepsilon_w = 0.59$ , but no longer for  $\varepsilon_w = 0.9$  (cf. also Sec. 3). Also in the case of nonzero  $\varepsilon_w$  a time of about  $\tau = 500$  MD time units suffices to establish the new liquid-vapor equilibrium, with more or less pronounced precursors of wetting layers at the walls of the slit pore, as described in Sec. 3. In view of our estimate of diffusion time scales in Sec. 4, this relatively fast establishment of equilibrium is perfectly reasonable.

One may also ask the question whether the time scale of equilibration depends on the  $z$ -coordinate across the film. Figs. 9, 10 indicate that such a dependence, if it exists, is very weak. One could expect, however, that such an effect should occur for much thicker slit pores under conditions, where the vapor density is lower in the center of the slit, while the precursors of the wetting layers then can be several particle diameters thick. In this situation, the relaxation time in the liquid layers adjacent to the walls could be much larger than in the vapor region. In our case, however, even for  $\varepsilon_w = 0.9$  where pronounced layering in the dense regions that build up close to the walls is observed (Fig. 10) no significant slowing

down has been detected.

## 5.2 Evaporation of Vapor into Vacuum

In the previous subsection we have considered the situation that for a slit pore completely filled with liquid an additional volume becomes available, into which evaporation can take place, and have presented data that illustrate how liquid-vapor interfaces form and a vapor-liquid phase equilibrium is established. In the present subsection, we consider the alternative scenario of a slit pore, in which such a vapor-liquid phase equilibrium already occurs, and by an external operation additional volume for the vapor phase becomes available. Of course, when the vapor spreads into the part of the volume which initially is empty, the average vapor density decreases, and the vapor no longer is in equilibrium with the liquid phase, with which it has coexisted in equilibrium for time  $t < 0$ . As a result, also liquid will evaporate again, driven by the density gradient that occurs in the vapor region, until the density in the whole region taken by the vapor has adjusted to the value the vapor density must have at coexistence with the liquid in thermal equilibrium at the chosen temperature and boundary conditions (i.e., value of  $\varepsilon_w$ ) at the walls of the confining slit pore.

Using the final equilibrium states for the system with linear dimensions  $L_x = 60$ ,  $L_y = 15$ ,  $L_z = 15$  with purely repulsive walls as an initial condition, we have increased the linear dimension in  $x$ -direction from  $L_x = 60$  to  $L_x = 72$ . Due to this rather modest increase of  $L_x$ , the liquid slab in the center of the system does not evaporate completely, but simply gets only a bit smaller, as a consideration of the average profile  $\rho(x, t)$  shows (Fig. 12). One sees that the strong density gradient (where originally the average density  $\rho(x, t = 0)$  jumps from about 0.092 to zero) at  $x = 6$  and  $x = 66$  (the vacuum takes the region  $0 \leq x < 6$  and  $66 < x \leq 72$  at  $t = 0$ ) smoothes out already during first 10 MD time units, and for  $t = 100$  the vapor density in the region  $0 \leq x < 12$  and  $60 < x \leq 72$  is almost independent of  $x$ , but the density in this region is distinctly smaller than the critical coexistence density. The thickness of the liquid slab has remained almost unchanged. Thus, in this initial regime of times it is basically the vapor present in the original system that has spread out into the empty region, which is understandable since the diffusion constant in the liquid region is much smaller, and also the driving force for evaporation of the liquid slab is clearly not very large. From Fig. 12 one can see that the shape of the interfacial profile (at least in its central part) does not change with time, it is only the interface position (which we may characterize precisely from the inflection point of  $\rho(x, t)$  in Fig. 12) that shifts in the time regime from  $t \approx 100$  to  $t \approx 500$  with approximately constant velocity, while for  $t \geq 500$  the vapor density for  $x \leq 12$  and  $x \geq 60$  starts to saturate, and then the interface velocity also decreases to zero.

As in the cases studied so far, we have again tried to obtain more detailed information on the spatially resolved data. At the slabs centered at  $x = 0.5$ , 12.5, 24.5 and 34.5 (all slabs have a width  $\Delta x = 1.0$ ) we have followed the time evolution of  $\rho(x, \bar{z}, t)$ , defining the positions  $\bar{z}$  of the 5 “slices” in  $z$ -direction in the same way as in the equilibrium case. Since 100 runs needed to be followed for 10000 MD time units, this part of the study involves a major computational effort, although the statistical fluctuations necessarily are still rather large (Fig. 13). One can see that for  $t \geq 2000$  there is no significant relaxation any more, while times  $t \leq 500$  clearly are not enough to fully establish equilibrium. While in the center of the interfacial region ( $x = 24.5$ ) the relaxation is slow but the density there decreases in a monotonic fashion, a nonmonotonic density relaxation occurs in the wings of the profile ( $x = 12.5$ ) far away from

the walls. In the regime closer to the walls (layers 1 and 2) the relaxation is always much faster, however.

### 5.3 Transient Diffusion during Evaporation Processes

It is possible in the simulation to ask the question how the presence of an evaporation process shows up in the time-dependence of the mean-square displacement of the particles. Experimentally, such a question could be asked e.g. for colloid-polymer mixtures [66], where a vapor liquid type phase separation occurs for suitable conditions, and it is possible to follow the motion of individual colloid particles with fluorescent labels [67]. In Fig. 14, we show representative results for the time-dependent diffusivities defined in Eqs. (5)- (8) for an evaporation simulation where  $L_x$  was changed from  $L_x = 30$  to  $L_x = 60$  at  $t = 0$ . Unlike the situation discussed in Sec. 4, where the choice of the origin of time did not play any role since the system in equilibrium obeys time translation invariance, this is no longer the case now: all quantities in Eqs. (5)- (8) depend on two times now, the time chosen for the origin  $t = 0$  there, and the time  $t$  elapsed since then. We have not attempted to study this non-stationary transport problem in full detail, however, but focus only on the case where the deviation from equilibrium is strongest, i.e. when the origin of time chosen in Eqs. (5)- (8) coincides with the time where the change of  $L_x$  is performed.

While the initial ballistic regime (where  $D(t) \propto t$ ) that one can recognize for  $1 \leq t \leq 6$  in Fig. 14, is not much affected by the fact that the system is out of equilibrium, for  $t > 6$  a very different behavior occurs:  $D^{(yz)}(t)$  becomes slower for some transient time period, while for  $t > 20$  another speed-up occurs, and near  $t = 100$  a maximum of  $D^{(yz)}(t)$  occurs, followed by a slow decay to the asymptotic value. The precise height and location of this maximum depend on the choice of  $\varepsilon_w$  slightly. All other time-dependent diffusion constants do contain also mean-square displacements in  $x$ -direction, and they show a strong speed up already at times  $t > 6$ . We attribute this speed up to the drift that occurs in  $x$ -direction: since it is more likely for the particles to move in  $x$ -direction than in any other direction,  $D^{(yz)}(t)$  exhibits a slower increase than in the ballistic regime. This nonequilibrium enhancement of  $D(t)$  and the various choices for  $D^{(\alpha\beta)}(t)$  [ $\alpha, \beta = x, y, z$ ] shown in Fig. 14 leads to maxima in most of the mean-square displacements that are more pronounced than the corresponding data in the confined pure phases in equilibrium (Fig. 6). The diffusion constants that the systems relax to, which show up as the flat plateaus in Fig. 14 for  $t \geq 2000$ , have values in between that of confined pure liquid and vapor phases, consistent with the (qualitative) expectation. Of course, we are far from a quantitative understanding of transport phenomena during relaxation in such inhomogeneous two-phase systems in confined geometry, however.

## 6 Conclusions

Fluids confined in slit-like pores can form liquid bridges coexisting with vapor at temperatures below the critical point. In the present work, we have studied for a simple Lennard-Jones model of a fluid the static structure of such liquid bridges, for several typical cases of fluid-wall interactions, corresponding to (incomplete) drying and wetting conditions. We have used molecular dynamics simulations to explore the partial (or complete) evaporation of such bridges resulting from changes of external thermodynamic control parameters and we have discussed the interplay of finite size effects (associated with the finite width of the slit pore, or with the finite linear dimensions of the liquid bridge in the directions parallel

to the slit walls, or both) and surface effects due to the walls.

When one considers the density variation in the direction perpendicular to the confining walls, one finds that both in the liquid phase and in the vapor phase the density approaches the values of bulk liquid and vapor at the coexistence curve, after about only 5 Lennard-Jones diameters, if one stays away from the region where liquid-vapor interfaces run across the slit pore (this condition also requires, of course, that the liquid bridge is thick enough that the two interfaces separating it from the vapor phase are non-interacting). This finding holds for all choices of the wall-fluid interaction (only when the slit width  $D$  gets several orders of magnitude larger than the Lennard-Jones diameter and if one is very close to conditions of complete wetting or complete drying, would be a larger inhomogeneity in the direction perpendicular to the wall expected). On the other hand, when the two interfaces between the liquid bridge and the vapor are close enough together so that their interaction cannot be neglected (e.g. the case  $\varepsilon_w = 0.9$  in Figs. 1, 3;  $\varepsilon_w = 0.7$  in Figs. 2, 3), the density inside the liquid bridge remains smaller than in the bulk, and one can observe a smooth crossover to the state where the liquid "bridge" rather should be described as two wall-attached droplets opposite of each other (Fig. 2,  $\varepsilon_w = 0.7$ ). Changing the thermodynamic conditions, in this way a smooth crossover from states containing a bridge to states without a bridge (Fig. 2,  $\varepsilon_w = 0.9$ ) are possible, and no sharp phase transitions (in the sense of a singular behavior of thermodynamic potentials or their derivatives) are involved, when all linear dimensions considered remain finite.

For the conditions studied, there is a significant (but not too strong) dynamic asymmetry between the coexisting phases in the bulk (the diffusion constant of the vapor is about 6 times larger than that of the liquid, Fig. 6). When one considers either pure vapor or pure liquid phases in confinement, the crossover from three-dimensional to quasi-two-dimensional diffusion already causes slow transients in the mean square displacements, Eq. (6) of the order of several thousand MD time units (physically, this may correspond to about 10 nanoseconds). It turns out that this time-scale associated with diffusion in confined geometry in equilibrium is larger than the time scale on which evaporation processes take place (Figs. 9- 13). Both the evaporation of liquid into vacuum and of vapor into vacuum is essentially completed after a few hundred MD time units already. When the vapor that evaporates into the vacuum still coexists with a liquid bridge in the center of the slit pore, the liquid bridge must somewhat shrink to maintain local thermal equilibrium: in this way the establishment of a density gradient in the vapor region of the system can be avoided. During the evaporation process, some of the mean-square displacements show super-diffusive behavior (Fig. 14).

Of course, our observations are only a first step towards the full clarification of the problem: it would be interesting to vary both parallel and perpendicular linear dimensions over at least a decade systematically, to clarify under which conditions the evaporation process becomes much slower (which then would be relevant for applications). Also a study of the variation with temperature would be interesting. However, all such extensions need substantial computer resources, and must be left to future work. However, we hope that the present work stimulates both the development of phenomenological analytical work and experimental studies on these issues.

**Acknowledgements:** The first author (K.B.) acknowledges financial support from the Alexander von Humboldt Foundation.

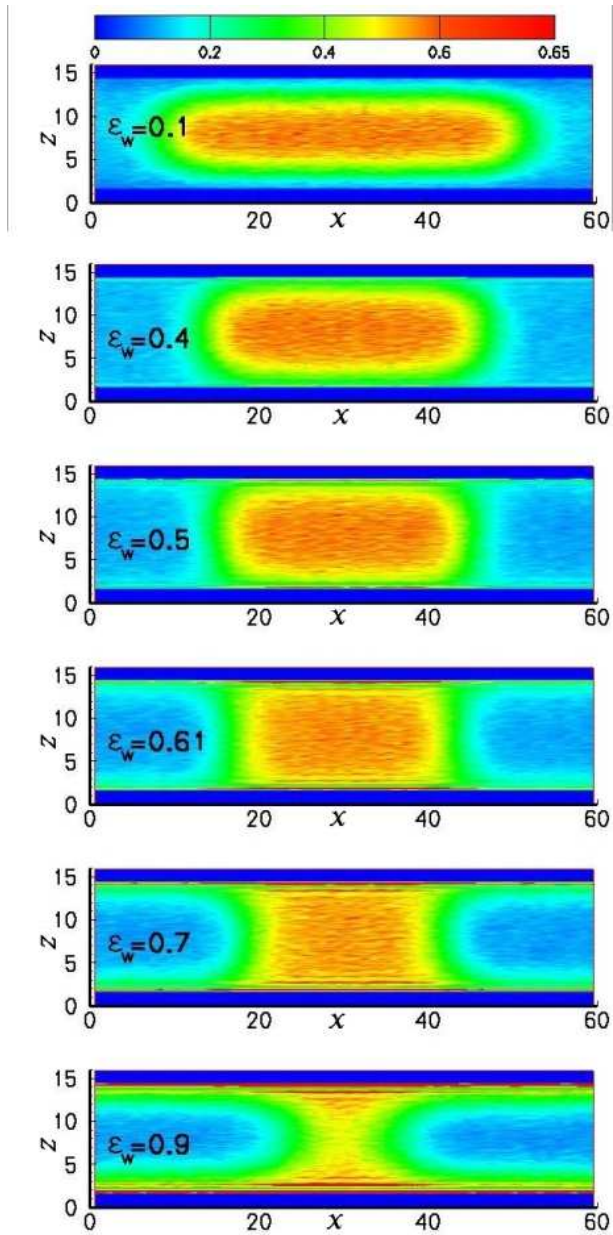


Figure 1: (Color) Density distribution  $\rho(x, z)$  for systems with linear dimensions  $L_x = 60$ ,  $L_y = 20$  and  $L_z = 16$ , for 6 values of  $\varepsilon_w = 0.1, 0.4, 0.5, 0.61, 0.7, 0.9$  (from top to bottom). The  $z$ -axis is oriented along the ordinate and the  $x$ -axis along the abscissa. The value of the density  $\rho$  corresponds to the color code, as shown by the bar on the right side of the plots. The temperature is  $T^* = k_B T / \varepsilon = 0.9366$ . The system was simulated for 20000 time units (cf. description in Sec. 2), and then averages were taken over last 15000 MD time units  $\tau$ .

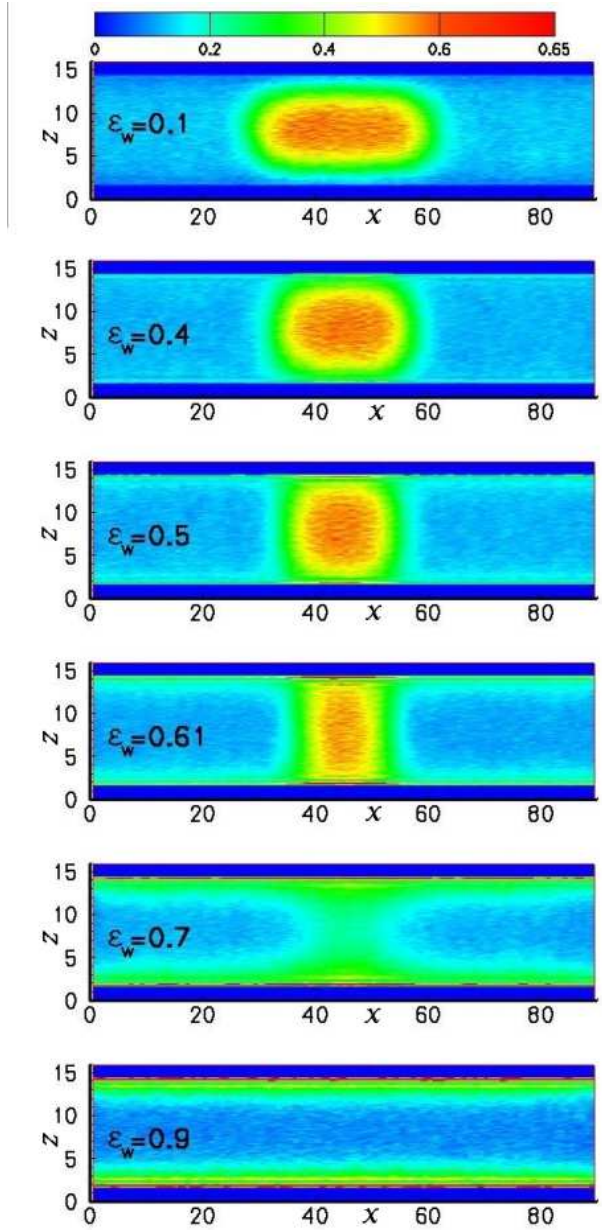


Figure 2: (Color) Same as Fig. 1, but for  $L_x = 90$  instead of  $L_x = 60$ . Note that the scale along the  $x$ -direction is compressed relative to the scale for the  $z$ -direction.

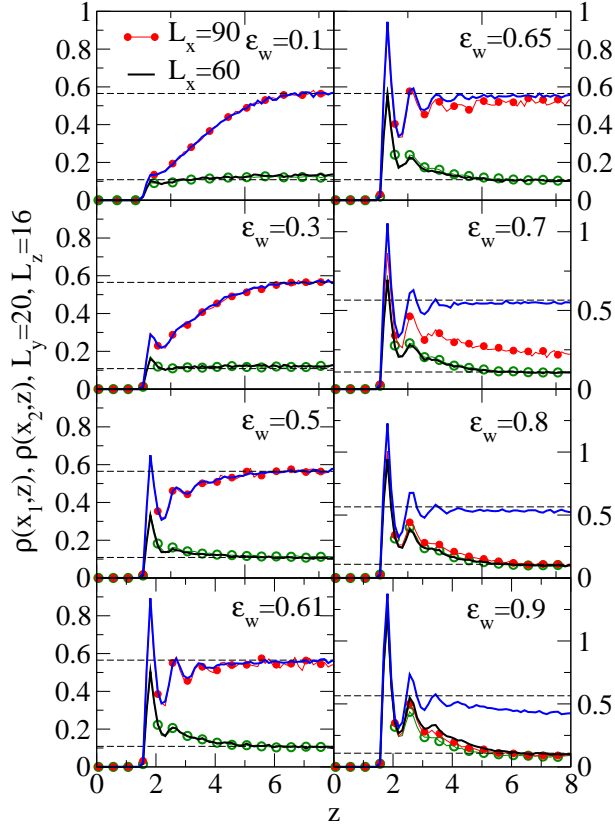


Figure 3: (Color online) Density profiles  $\rho(x_1, z)$  and  $\rho(x_2, z)$  plotted vs.  $z$  for 8 values of  $\varepsilon_w = 0.1, 0.3, 0.5, 0.61$  (from top to bottom, left column) and  $\varepsilon_w = 0.65, 0.7, 0.8, 0.9$  (from top to bottom, right column). Solid lines and lines with circles represent density profiles for the system  $60 \times 20 \times 16$  (cf. Fig. 1) and  $90 \times 20 \times 16$  (cf. Fig. 2), respectively. In each frame of the panel the upper curve shows  $\rho(z, x_1)$  with  $x_1$  being defined via  $\rho(x_1, z) = \int_{25}^{35} \rho(x, z) dx / 2$ , and the lower curve shows  $\rho(x_2, z)$ , with  $x_2$  being defined via  $\rho(x_2, z) = [\int_0^3 \rho(x, z) dx + \int_{57}^{60} \rho(x, z) dx] / 6$ . Thus, the upper curve shows the density profile along a cut through the center of the liquid slab, while the lower curve shows the density profile through the vapor region far away from the vapor-liquid interface. These averages are carried out for time above  $t > 5000$  over 15000 MD time units  $\tau$ . Horizontal broken straight lines show bulk  $\rho_l$  and  $\rho_g$ , respectively.

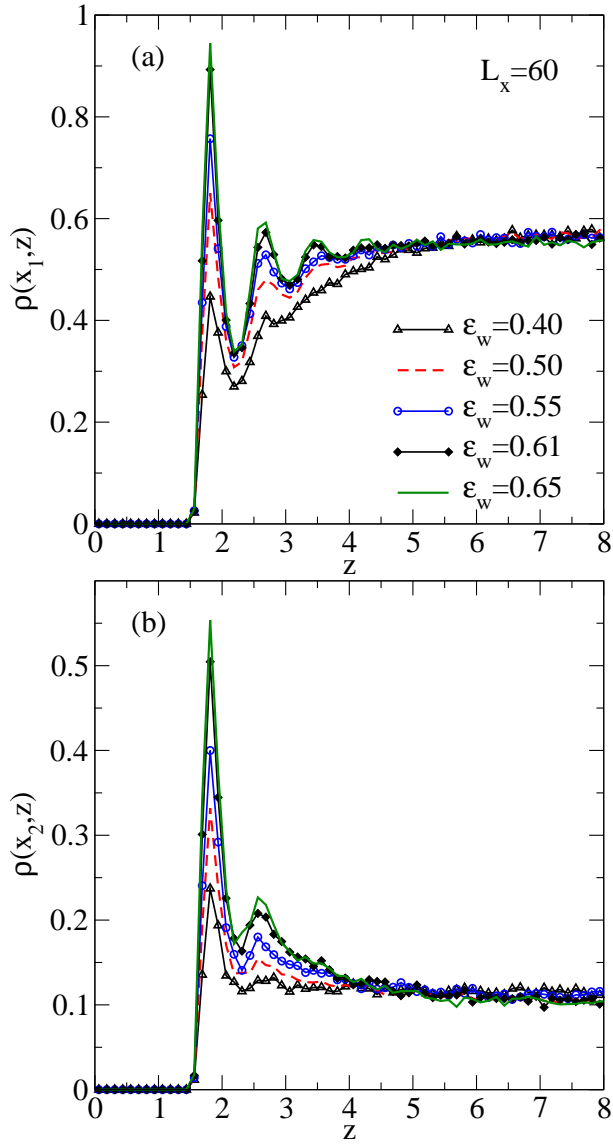


Figure 4: (Color online) Magnified plot of finely resolved density profiles in liquid  $\rho(x_1, z)$  (a) and vapor  $\rho(x_2, z)$  (b) plotted vs.  $z$  for  $\epsilon_w = 0.4, 0.5, 0.55, 0.61$  and  $0.65$ , as indicated in the figure, for  $L_x = 60$ , all other parameters being the same as in Figs. 1-3. Note that the cells for the averaging have a width  $\Delta z = 0.125$  in  $z$ -direction.



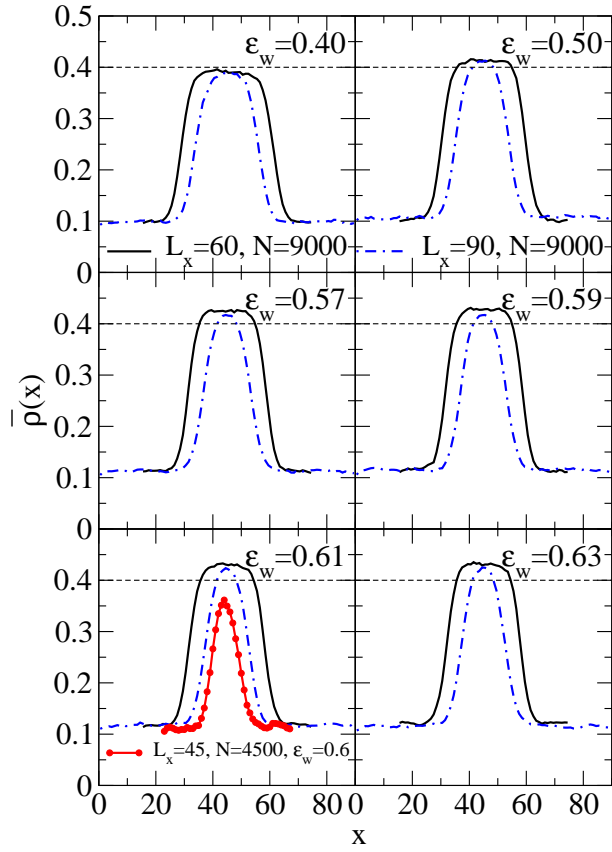


Figure 5: (Color online) Density profiles  $\bar{\rho}(x)$  averaged in  $z$ -direction plotted vs.  $x$  for  $L_x = 60$  and  $L_x = 90$ , for 6 values of  $\varepsilon_w$ , as indicated

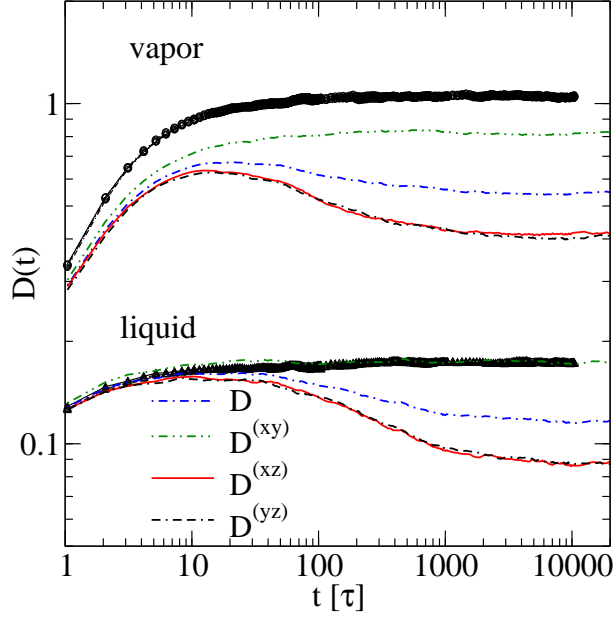


Figure 6: (Color online) Log-log plot of time-dependent diffusion constants  $D(t)$ ,  $D^{(xy)}(t)$ ,  $D^{(xz)}(t)$  and  $D^{(yz)}(t)$  vs. time, for systems at  $T^* = 0.9366$  both in the vapor phase (which in the bulk has a density  $\rho = 0.10866$ ) and in the liquid phase (which in the bulk has a density  $\rho = 0.565032$ ). Both data for bulk systems (linear dimensions  $27 \times 20 \times 16$  for the pure liquid at coexistence and  $140 \times 20 \times 16$  for the pure vapor phase at coexistence, with periodic boundary conditions in all three directions) and for confined systems in single-phase states (confined by walls with  $\varepsilon_w = 0.59$ , choosing linear dimensions  $34 \times 20 \times 16$  for the liquid and  $240 \times 20 \times 16$  for the vapor) are included. Lines with circles correspond to bulk results for vapor, lines with triangles - to bulk results for liquid. Lines without symbols correspond to data for confined systems.

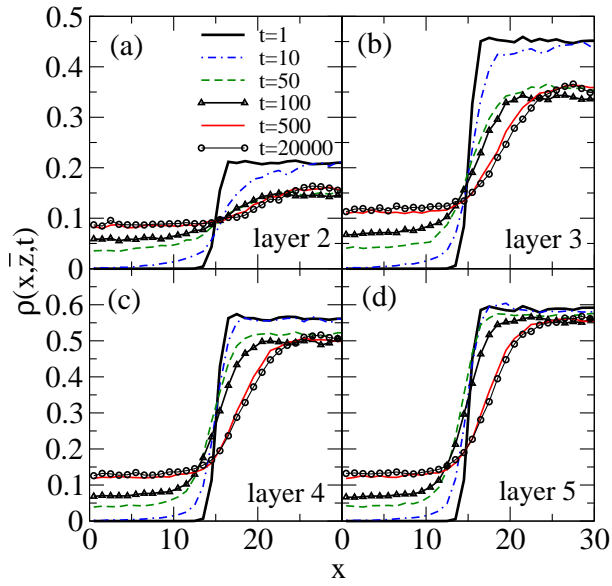


Figure 7: (Color online) Time evolution of the average density  $\rho(x, \bar{z}, t)$  during the evaporation of liquid into vacuum after the change of linear dimension  $L_x = 30$  to  $L_x = 60$  for layer 2 (a), 3 (b), 4 (c) and 5 (d). The region of  $z$  over which  $\rho(x, z, t)$  is averaged in the different layers is explained in the main text. Different curves indicate time  $t$  after the volume change, as indicated. These data result from averaging over 100 independent and equivalent runs.

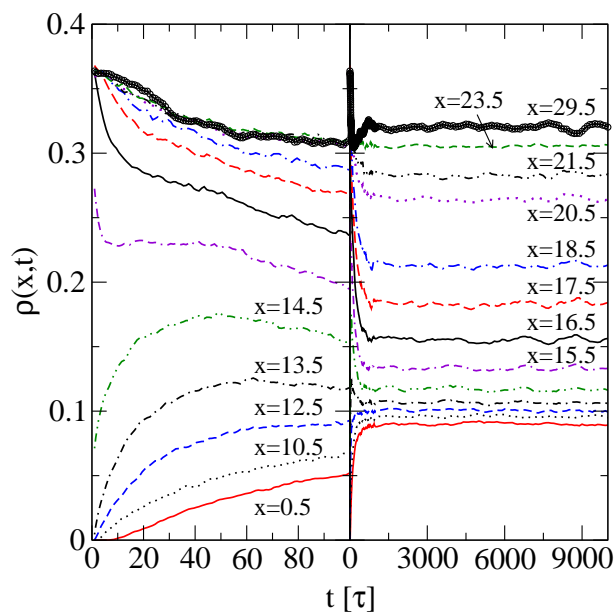


Figure 8: (Color online) Evaporation of liquid into vacuum. Time dependence of the density  $\rho(x,t)$  averaged in  $z$ -direction plotted versus time for short time scales (left part) and over long times (right part). Different curves show a few values of  $x$ , as indicated in the figure.

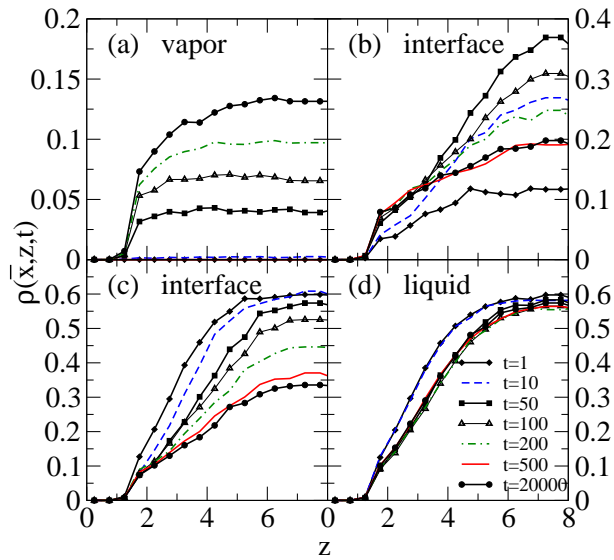


Figure 9: (Color online) Profiles  $\rho(\bar{x}, z, t)$  plotted vs.  $z$  for  $x$  averaged from 0 to 3 and 57 to 60 (a), from 14 to 15 and 45 to 46 (b), from 17 to 18 and 47 to 48 (c) and from 27 to 33 (c).

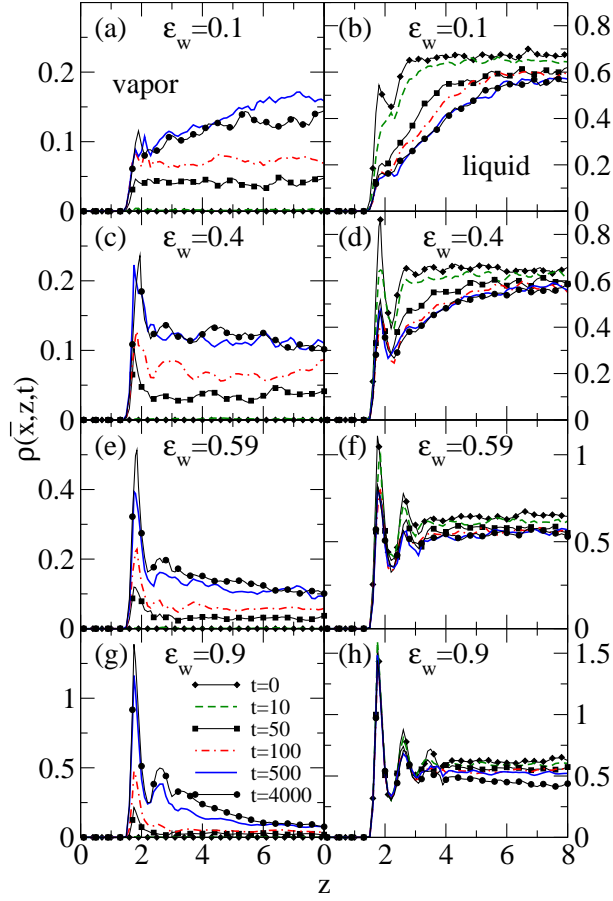


Figure 10: (Color online) Profiles  $\rho(\bar{x}, z, t)$  plotted vs.  $z$  for  $x$  averaged from 0 to 5 and 55 to 60 (left column) and from 25 to 35 (right column), for  $\varepsilon_w = 0.1$  (a,b),  $\varepsilon_w = 0.4$  (c,d),  $\varepsilon_w = 0.59$  (e,f) and  $\varepsilon_w = 0.9$  (g,h) choosing now a box of linear dimensions  $60 \times 20 \times 16$ , and different times  $t$  as indicated, after a change of  $L_x$  from  $L_x = 30$  to  $L_x = 60$  was performed.

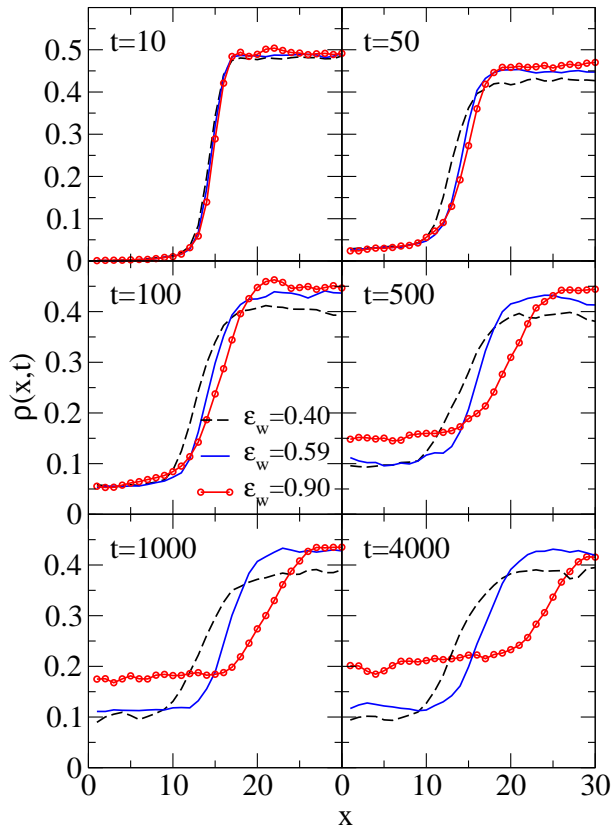


Figure 11: (Color online) Total density  $\rho(x,t)$  averaged over the  $z$ -direction across the slit pore, for a box of linear dimensions  $L_x \times 20 \times 16$ , at times  $t$  after at time  $t = 0$  a change of  $L_x$  from  $L_x = 30$  to  $L_x = 60$  was performed. Three choices of  $\varepsilon_w$  are shown:  $\varepsilon_w = 0.4, 0.59$  and  $0.9$ .

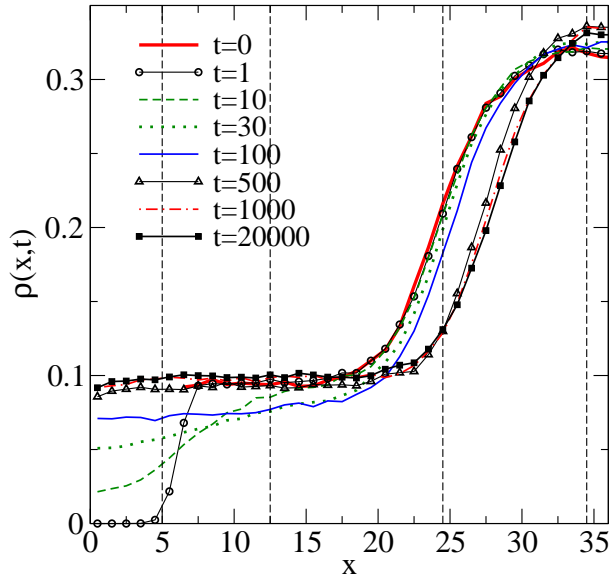


Figure 12: (Color online) Time dependence of the density  $\rho(x, t)$  averaged in the  $z$ -direction across the slit pore, for a system of size  $L_x \times 15 \times 15$ , for which at time  $t = 0$  a change from  $L_x = 60$  to  $L_x = 72$  is performed (evaporation of coexisting liquid and vapor into vacuum). The interaction between the particles forming the walls and the fluid particles is purely repulsive. Different curves indicate the various times, as indicated. The vertical straight lines highlight the positions (see text) where the spatially resolved time dependence is analyzed in Fig. 13.



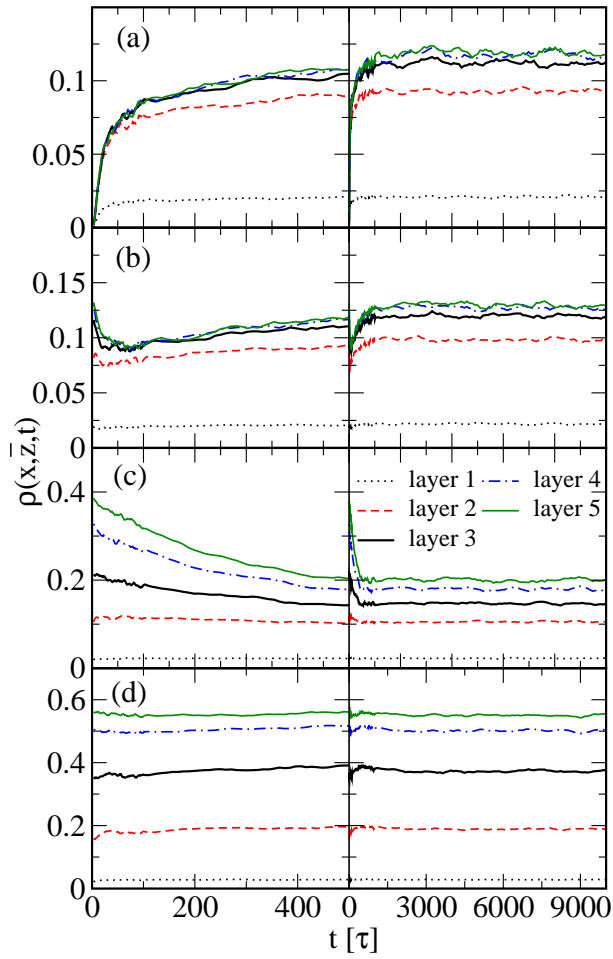


Figure 13: (Color online) Plot of  $\rho(x, \bar{z}, t)$  vs.  $t$  for  $x = 0.5$  (a), 12.5(b), 24.5 (c) and 34.5 (d). Each panel shows five values of  $\bar{z}$ , as indicated in part (c). The left part shows always the initial relaxation ( $0 \leq t \leq 500$ ), the right part shows the full interval of times ( $0 \leq t \leq 10000$ ) over which the simulations were extended. For further explanations see text.

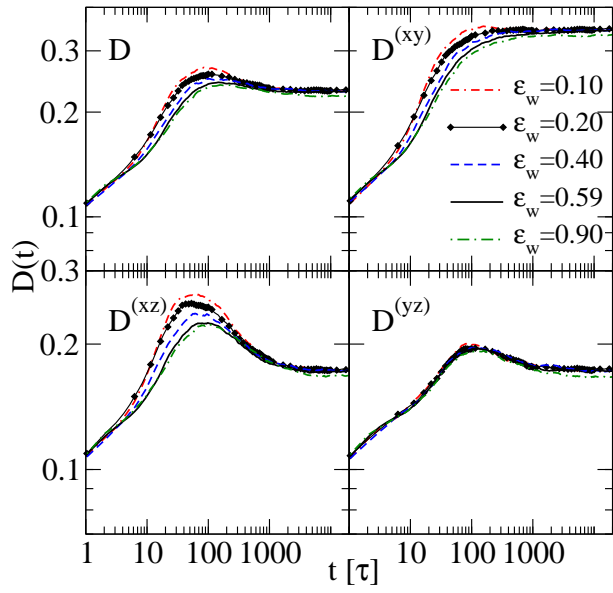


Figure 14: (Color online) Effective time-dependent diffusion constants  $D(t)$ ,  $D^{(xy)}(t)$ ,  $D^{(xz)}(t)$  and  $D^{(yz)}(t)$  plotted vs. time on a log-log plot, for several choices of  $\varepsilon_w$ , as indicated. The origin of time  $t = 0$  used in the definitions, Eqs. (5)- (8), was chosen coincident with the change from  $L_x = 30$  to  $L_x = 60$ , where evaporation of the confined liquid into vacuum starts.

## References

- [1] H. J. Herrmann, J.-P. Hovi, and S. Luding (eds) *The Physics of Granular Media* (Kluwer Acad. Publ., Dordrecht, 1998)
- [2] F. Schüth, K.S.W. Sing, and J. Weitkamp (Eds.) *Handbook of Porous Solids* (Wiley-VCH, Weinheim, 2002)
- [3] S.M. Auerbach, K.A. Carrado, and P.K. Dutta (Eds.) *Handbook of Zeolite Science and Technology* (Marcel Dekker, New York, 2003)
- [4] I. Turner and A.S. Mujumdar (eds) *Mathematical Modeling and Numerical Techniques in Drying Technology* (Marcel Dekker, New York, 1997)
- [5] Y. Gogotsi, J.A. Libera, A. Güvenç-Yazicioglu, and C.M. Megaridis, *Appl. Phys. Lett.* **79**, 1021 (2001)
- [6] R.D. Piner, J. Zhu, F. Xu, S. Hong, and C.A. Mirkin, *Science* **283**, 661 (1999)
- [7] J. Klein and E. Kumacheva, *Science* **269**, 816 (1995)
- [8] M. Alawa, M. Dubé, and M. Rost, *Adv. Phys.* **53**, 83 (2004)
- [9] L.D. Gelb, K.E. Gubbins, R. Radhakrishnan, and M. Sliwiska-Bartkowiak, *Rep. Progr. Phys.* **62**, 1573 (1999)
- [10] A. Meller, *J. Phys.: Condens. Matter* **15**, R581 (2003)
- [11] T.M. Squires and S.R. Quake, *Rev. Mod. Phys.* **77**, 977 (2005)
- [12] M. Schoen and S. Klapp, *Rev. Comp. Chem.* **24**, 1 (2007)
- [13] P. Huber, S. Grüner, C. Schäfer, K. Knorr, and A.V. Kityk, *Eur. Phys. J. Spec. Topics* **141**, 101 (2007)
- [14] K.M. van Delft, J.C.T. Eijkel, D. Mijatovic, T.S. Druzhinina, H. Rathgen, N.R. Tas, A. van den Berg, and F. Mugele, *Nano Lett.* **7**, 345 (2007)
- [15] D.I. Dimitrov, A. Milchev, and K. Binder, *Phys. Rev. Lett.* **99**, 054501 (2007)
- [16] M. Rost, L. Laurson, M. Dubé, and M. Alava, *Phys. Rev. Lett.* **98**, 054502 (2007)
- [17] D.I. Dimitrov, L.I. Klushin, A. Milchev, and K. Binder, *Phys. Fluids* **20**, 092102 (2008)
- [18] S. Puri and K. Binder, *J. Stat. Phys.* **77**, 145 (1994)
- [19] K. Binder, *J. Nonequil. Thermodynamics* **23**, 1 (1998)
- [20] S. Puri, *J. Phys.: Condens. Matter* **17**, R101 (2005)
- [21] S.K. Das, S. Puri, J. Horbach, and K. Binder, *Phys. Rev. Lett.* **96**, 016107 (2006); *Phys. Rev. E* **73**, 031604 (2006)
- [22] K. Bucior, L. Yelash, and K. Binder, *Phys. Rev. E* **77**, 051602 (2008)

- [23] A. Lofti and J. Fischer, Ber. Bunsenges. Phys. Chem. **94**, 233 (1990)
- [24] M. Matsumoto, K. Yasuoka, and Y. Kataoka, Fluid Phase Equil. **104**, 431 (1995)
- [25] M. Matsumoto, Fluid Phase Equil. **125**, 195 (1996); *ibid.* **144**, 307 (1998)
- [26] M. Matsumoto and S. Fuijkawa, Microscale Thermophysical Engineering **1**, 119 (1997)
- [27] V.V. Zhakhovskii and S.I. Anisimov, JETP **84**, 734 (1997)
- [28] S.I. Anisimov, D.O. Dunikov, V.V. Zhakhovskii, and S.P. Matyshenko, J. Chem. Phys. **110**, 8722 (1999)
- [29] Z.-J. Wang, M. Chen, and Z.-Y. Guo, Microscale Thermophys. Eng. **7**, 275 (2003)
- [30] A.P. Bhansali, Y. Bayazitoglu, and S. Maruyama, Int. J. Therm. Sci. **38**, 66 (1999)
- [31] J.H. Walther and P. Koumoutsakos, J. Heat Transfer **123**, 741 (2001)
- [32] M.M. Micci, T.L. Kaltz, and L.N. Long, Atomization and Sprays **11**, 653 (2001)
- [33] S. Sumardiono and J. Fischer, Int. J. Heat and Mass Transfer **49**, 1148 (2006)
- [34] K. Binder and M.H. Kalos, J. Stat. Phys. **22**, 363 (1980)
- [35] H. Furukawa and K. Binder, Phys. Rev. A **26**, 556 (1982)
- [36] S. Varga, D. Boda, D. Henderson, and S. Sokolowski, J. Coll. Int. Sci. **227**, 223 (2000)
- [37] K. Binder, Physica A **319**, 99 (2003)
- [38] L.G. MacDowell, P. Virnau, M. Müller, and K. Binder, J. Chem. Phys. **120**, 5293 (2004)
- [39] L. Salamacha, A. Patrykiewicz, S. Sokolowski, and K. Binder, J. Chem. Phys. **122**, 074703 (2005)
- [40] I. Brovchenko, A. Geiger, and A. Oleinikova, Eur. Phys. JB **44**, 345 (2005)
- [41] N. Giovambattista, P.J. Rossky, and P.G. Debenedetti, Phys. Rev. E **73**, 041604 (2006)
- [42] K. Yasuoka, G.T. Gao and X. C. Zeng, J. Chem. Phys. **112**, 4279 (2000)
- [43] V. Talanquer and D.W. Oxtoby, J. Chem. Phys. **114**, 2793 (2001)
- [44] J. Yaneva, A. Milchev, and K. Binder, J. Chem. Phys. **121**, 12632 (2004)
- [45] J. Yaneva, A. Milchev, and K. Binder, J. Phys.: Condens. Matter **17**, S4199 (2005)
- [46] A. Valencia, M. Brinkmann, and R. Lipowsky, Langmuir **17**, 3390 (2001)
- [47] R. Lipowsky, M. Brinkmann, R. Dinova, T. Franke, J. Kierfeld, and X. Zhang, J. Phys.: Condens. Matter **17**, S537 (2005)
- [48] M.P. Allen and D.J. Tildesley, *Computer Simulation of Liquids* (Clarendon Press, Oxford, 1987)
- [49] D.C. Rapaport, *The Art of Molecular Dynamics Simulation* (Cambridge Univ. Press, Cambridge, 1995)

- [50] K. Binder and G. Ciccotti (eds) *Monte Carlo and Molecular Dynamics of Condensed Matter* (Italian Physical Society, Bologna, 1996)
- [51] P.G. deGennes, *Rev. Mod. Phys.* **57**, 825 (1985)
- [52] D.E. Sullivan and M.M. Telo da Gama, in *Fluid Interfacial Phenomena* (C.A. Croxton, ed.) p. 45 (Wiley, New York, 1986)
- [53] S. Dietrich, in *Phase Transitions and Critical Phenomena, Vol 12* (C. Domb and J.L. Lebowitz eds.) p. 1 (Academic, New York, 1988)
- [54] M. Schick, in *Liquids at Interfaces* (J. Charvolin, J.-F. Joanny, and J. Zinn-Justin, eds.) p. 415 (North-Holland, Amsterdam, 1990)
- [55] G. Forgacs, R. Lipowsky, and T.M. Nieuwenhuizen, in *Phase Transitions and Critical Phenomena, Vol. 14* (C. Domb and J.L. Lebowitz, eds.) Chapter 2 (Academic Press, London, 1991)
- [56] D. Bonn and D. Ross, *Rep. Progr. Phys.* **64**, 1085 (2001)
- [57] B.M. Mognetti, L. Yelash, P. Virnau, W. Paul, K. Binder, M. Müller, and L.G. MacDowell, *J. Chem. Phys.* **128**, 104501 (2008)
- [58] P. Virnau, M. Müller, L.G. MacDowell, and K. Binder, *J. Chem. Phys.* **121**, 2169 (2004)
- [59] K. Binder, *Rep. Progr. Phys.* **60**, 487 (1997)
- [60] A. Werner, F. Schmid, M. Müller, and K. Binder, *J. Chem. Phys.* **107**, 8175 (1997)
- [61] L.G. MacDowell, V.K. Shen, J.R. Errington, *J. Chem. Phys.* **125**, 034705 (2006)
- [62] D. Jasnow, *Rep. Progr. Phys.* **47**, 1059 (1984)
- [63] <http://www.espresso.mpg.de>; for a description see also H.-J. Limbach, A. Arnold, B.A. Mann, C. Holm, *Comput. Phys. Commun.* **174**, 704 (2006)
- [64] K. Binder, M. Müller, and D.P. Landau, *J. Stat. Phys.* **110**, 1411 (2003)
- [65] H. Bock, K. E. Gubbins, and M. Schoen, *J. Phys. Chem. C* **111**, 15493 (2007)
- [66] W. Poon, *J. Phys.: Condens. Matter* **14**, R859 (2002)
- [67] A. V. Blaaderen, *Prog. Colloid Polym. Sci.* **104**, 59 (1997)